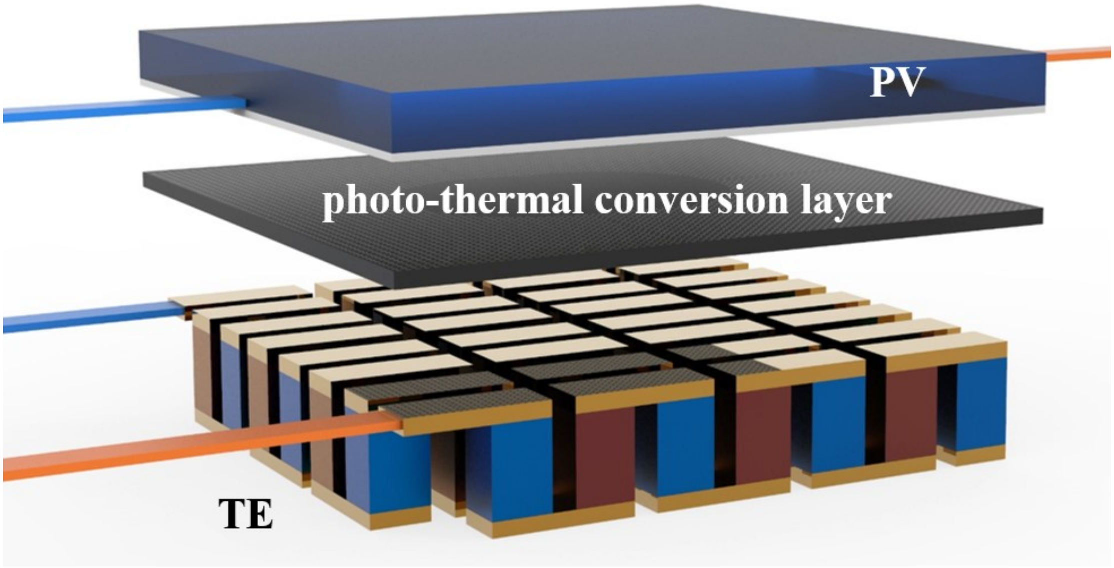

Fig S1. Separate systems.

The photothermal conversion layer (PCL) between PV and TE is separated, and PV and TE are in direct contact.

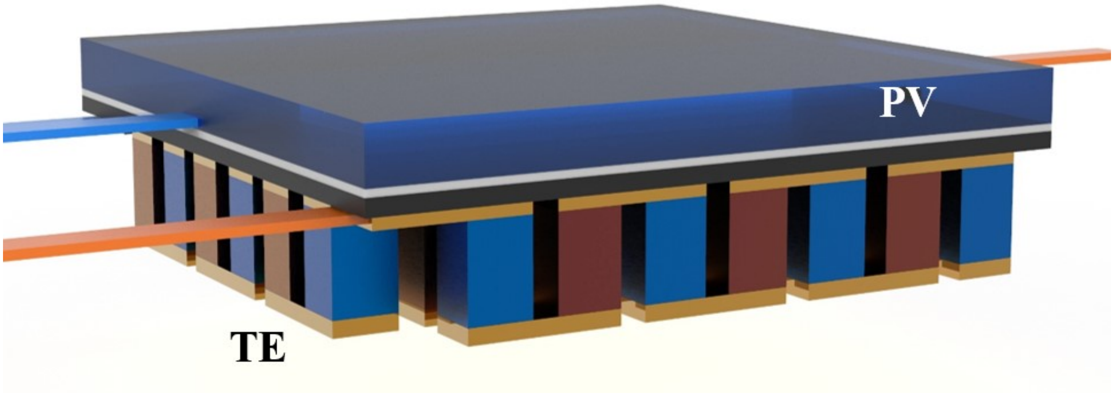

Fig S2. Integrated systems.

A photothermal conversion layer is integrated between the PV and TE to enhance the heat transfer between the PV and TE and to absorb the photon energy transmitted through the PV and convert it into thermal energy. The photothermal conversion layer is a VACNT-PMMA composite film, and the specific preparation method is described in Section 5.

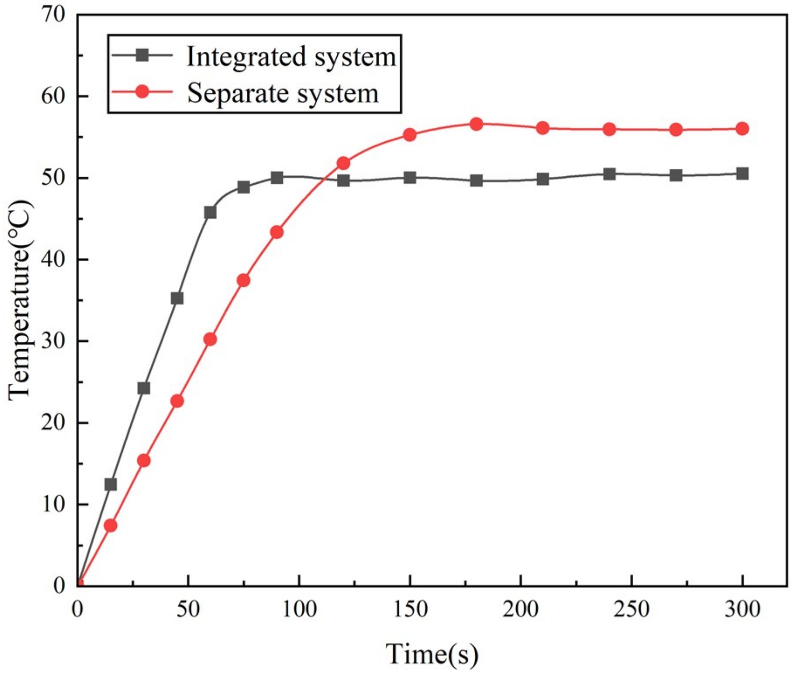

Fig S3. PV temperature response with heating time.

As can be seen from the figure, with the addition of the PCL, the heat loss during the transfer of heat in each component is reduced, the PV thermal response is faster, and the time to reach the maximum temperature is 30 s faster than that without the PCL. The addition of the equalization plate can solve the problem of heat concentration, and the maximum temperature of the PV is reduced ~5.5°C.

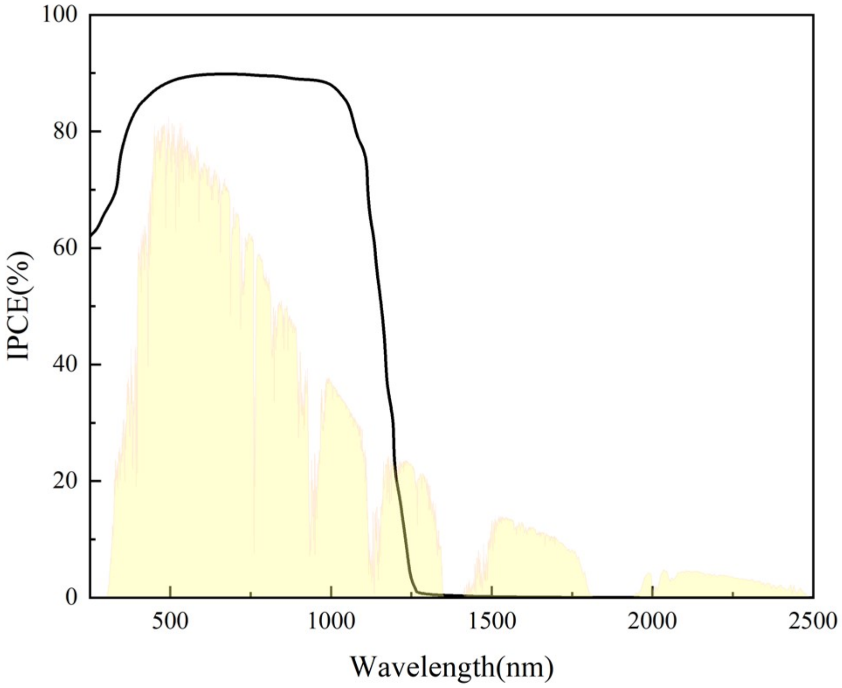

Fig S4. Incident photo-electron conversion efficiency (IPCE) of PV cells.

At photon wavelengths of 0-400 nm, the IPCE of silicon PV cells increases with wavelength, stabilizes and achieves a maximum value of 85% at wavelengths of 400-1200 nm, and then decreases steeply to zero as the photon wavelength continues to increase.

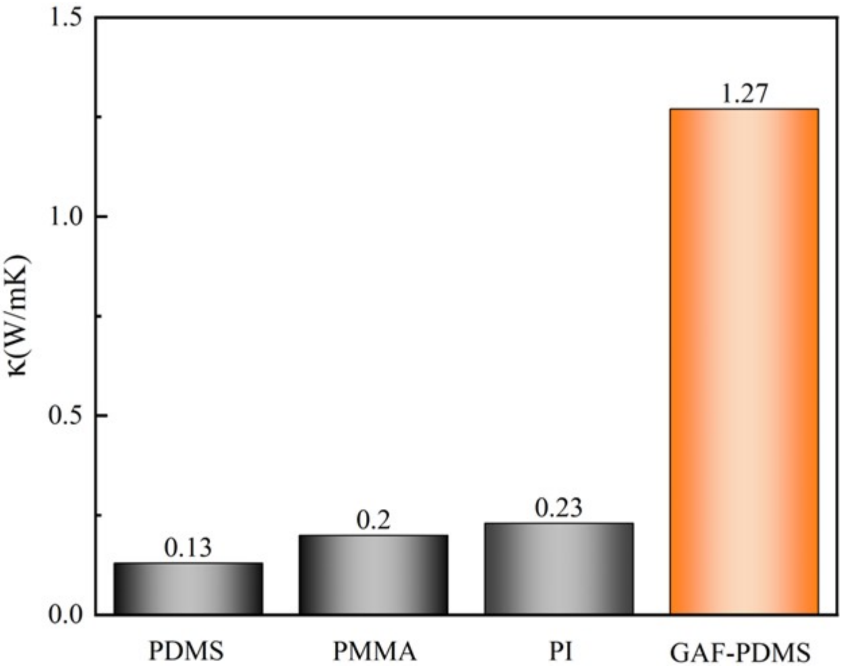

Fig S5. Discussion on RC thermal conductivity

The thermal conductivities of the organics-based radiative-cooled films PDMS, PMMA and PI are very low, only 1/10, 1/6 and 1/5 of the thermal conductivity of GAF-PDMS, respectively. The low thermal conductivity makes the heat conduction between RC and TE ineffective, and no efficient heat flow channel is established between RC film and TE surface, resulting in heat concentration or uneven temperature. The low thermal conductivity of the RC wastes the cooling energy, and the thermal concentration problem is detrimental to the power output of the TEG and the efficiency of the PV cell. The selection of GAF-PDMS film, which has a much higher thermal conductivity than RC and is also flexible, can greatly improve the heat transfer efficiency. Moreover, GAF has high thermal conductivity and transverse thermal conductivity so that the heat can be uniformly transferred to each position, avoiding heat loss and heat concentration problems, stabilizing the output power of TEG and improving the effect of PV thermal management.

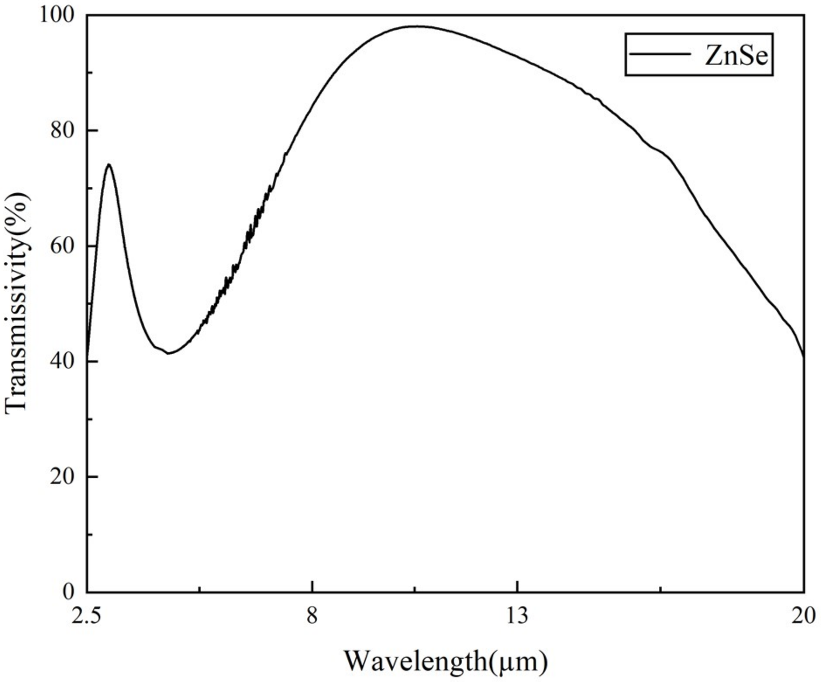

Fig S6. Transmission spectra of ZnSe glass.

The ZnSe glass has the advantage of high transmittance and, as can be seen from the figure, has greater transmittance in the 8-13 μm than at other wavelengths, peaking at 97%, and is virtually transparent in the atmospheric window band. Therefore, the ZnSe glass has almost no blocking effect on the thermal radiation emitted by the RC to outer space, and the RC still maintains good cooling effect. The combination of the ZnSe glass and the vacuum chamber can minimize the heat exchange between the PV-TE-RC and the environment and reduce the convective heat loss without blocking the RC's emission of thermal radiation to outer space.

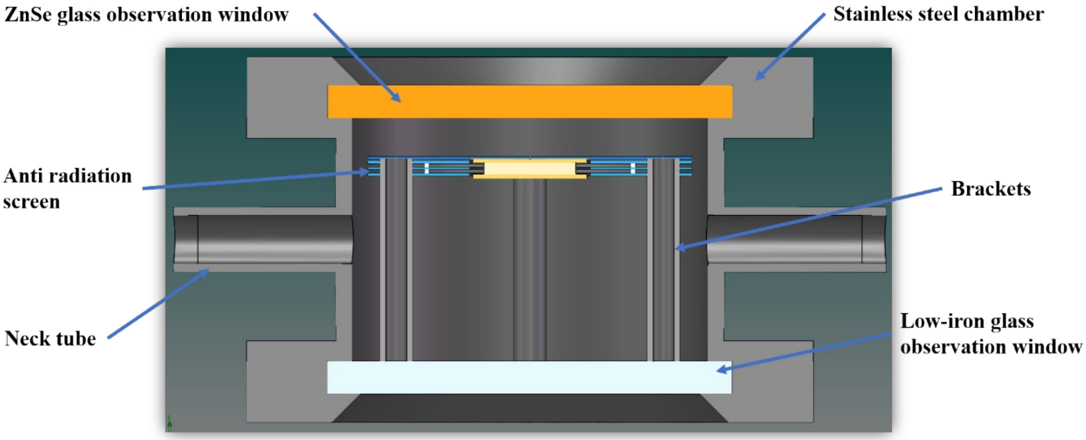

Fig S7. Vacuum cavity structure and PV-TE-RC arrangement.

The vacuum device mainly consists of vacuum chamber, observation window and vacuum pump. The PV-TE-RC generator is supported by hollow quartz posts and shielded by infrared reflective aluminum radiation. The vacuum chamber structure is shown in Fig. S7, which mainly consists of a ZnSe glass observation window, a stainless steel chamber, a bracket, a low-iron glass and neck tube. For specific parameters of the vacuum unit, see Section4.

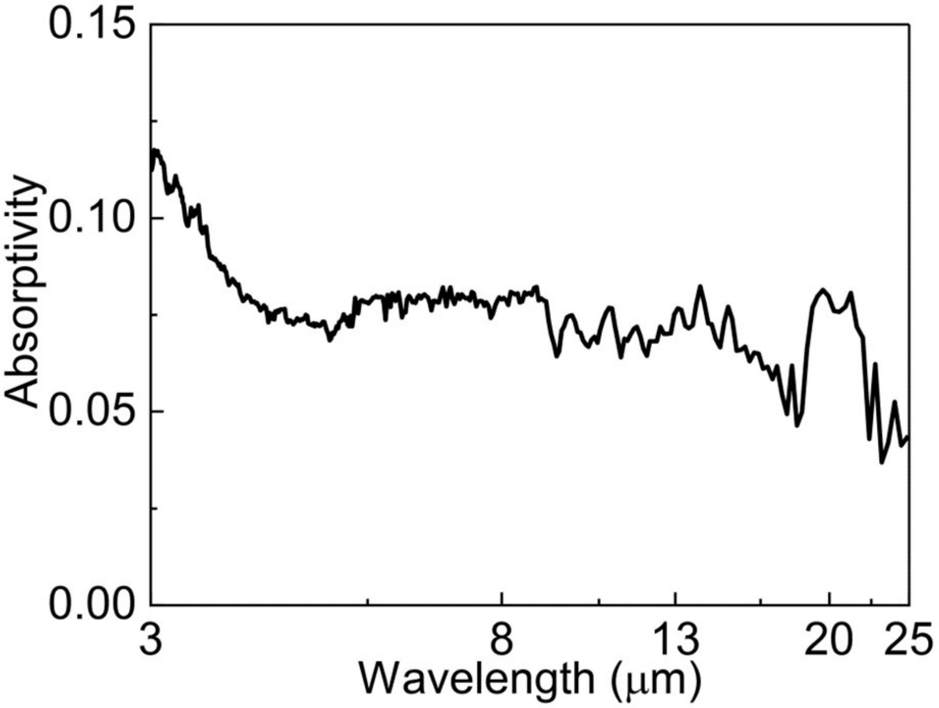

Fig S8. Optical property of Al radiation shield in the MIR region.

As can be seen from the figure, the polished aluminum plate has a low absorption rate for light in the MIR band and can reflect most of the infrared radiation. Therefore, the combination of multiple polished aluminum panels can reduce the radiation heat transfer between the reverse side of the sample and the inner wall of the vacuum chamber, reducing the heat loss of the system.

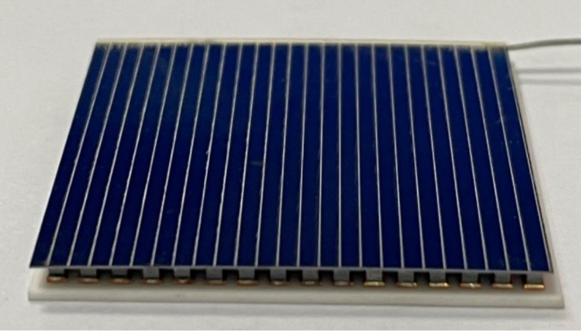

Fig S9. PV-TE-RC module physical diagram.

The PV-TE-RC module consists of a radiation cooler, a thermoelectric panel, a LCE and an Infrared-Transparent Si PV Cell.

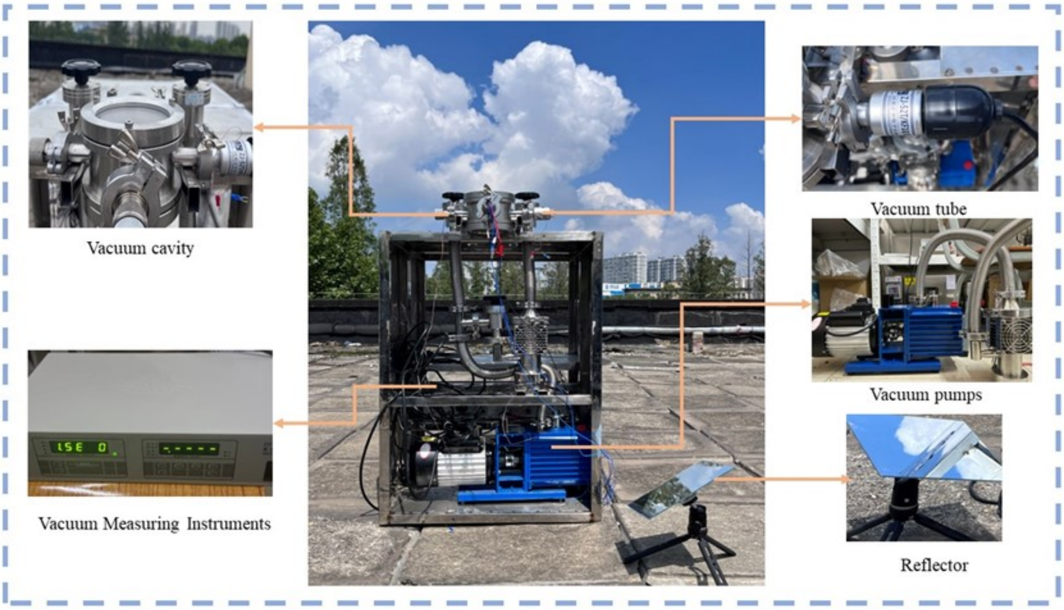

Fig S10. Outdoor experimental test system layout.

An outdoor experiment was conducted on consecutive summer days in Wuhan, China (30 '33 "N, 114' 21" E) to explore the comprehensive performance of PV-TE-RC under realistic weather conditions. The test system is mainly composed of self-made vacuum device, vacuum chamber, vacuum pump, reflector, data acquisition instrument and PV-TE-RC module. The test site is located on the roof without shelter, and the weather includes sunny and cloudy days.

Section1. Theoretical model of PV-TE-RC

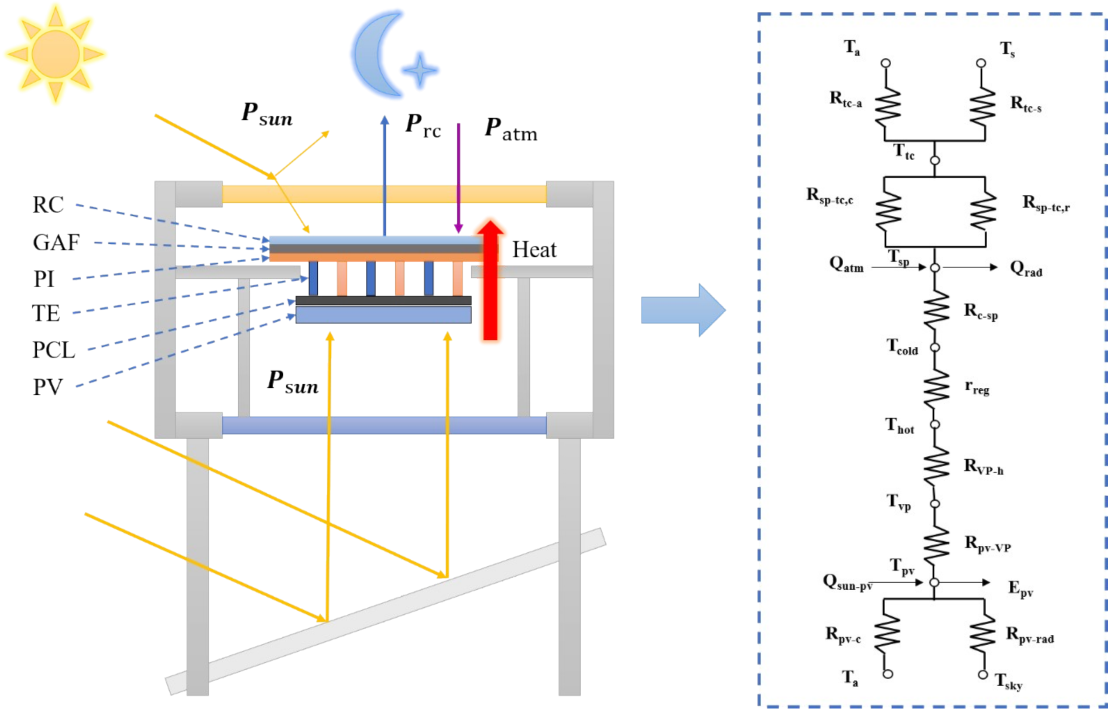

Fig S11. Theoretical model of PV-TE-RC system.

The model is based on the following assumed characteristics: (a) The characteristic parameters of each component remain unchanged; (b) Ignore the specific heat capacity of each component; (c) The temperature of each component is uniform in different directions; (d) The spectral characteristics of each component are independent of the angle.

(1) For the radiative cooler with transparent cover, the heat transfer mechanism is as follows [1]:

$$\frac{T_a-T_{tc}}{R_{tc-a}}+\frac{T_s-T_{tc}}{R_{tc-s}}+\frac{T_{sp}-T_{tc}}{R_{sp-tc,r}}+\frac{T_{sp}-T_{tc}}{R_{sp-tc,c}}+\alpha_{tc}GA_{tc}=0$$ * MERGEFORMAT

(3-1)

where R_{tc-a} and R_{tc-s} are the thermal resistance of the convection heat transfer between transparent cover and ambient air and the radiation heat transfer between transparent cover and sky, K/W; $R_{sp-tc,c}$and $R_{sp-tc,r}$ are the thermal resistance of the convection and radiation heat transfer between the sample plate and transparent cover, K/ W; T_a, T_s, T_{tc}, T_{sp} are respectively the temperature of ambient air, sky, transparent cover and radiative cooler, K; α_{tc} and A_{tc} are the absorptivity and area of transparent cover; G is the solar irradiance, W/m^2. Overall thermal resistance can be obtained from [2, 3],

$$R_{tc-a}=\frac{1}{(2.8+3u)A_{tc}}$$ * MERGEFORMAT (3-2)

$$R_{tc-s}=\frac{1}{\varepsilon_{tc}\sigma(T_{tc}^2+T_s^2)(T_{tc}+T_s)A_{tc}}$$ * MERGEFORMAT (3-3)

$$R_{sp-tc,r}=\frac{\frac{1}{\varepsilon_{sp}}+\frac{1}{\varepsilon_{tc}}-1}{\sigma(T_{sp}^2+T_{tc}^2)(T_{sp}+T_{tc})A_{sp}}$$ * MERGEFORMAT (3-4)

$$R_{sp-tc,c}=\frac{1}{A_{tc}h_{sp-tc,c}}$$ * MERGEFORMAT (3-5)

$$h_{sp-tc,c}=\frac{Nu\cdot K_{air}}{H}$$ * MERGEFORMAT (3-6)

where u is the wind speed, m/s; A_{tc} and A_{sp} are the area of transparent cover and the sample plate, m^2; ε_{tc} and ε_{sp} are the total, hemispherical emissivity respectively; σ is Boltzmann constant, W/(m^2·K^4); K_{air} is the thermal conductivity of air, W/(m·K); $h_{sp-tc,c}$ is the internal air natural convection heat transfer coefficient, W/(m^2·K); H is the thickness of air interlayer in the device, m.

(2) For the sample plate, the energy balance equation is as follows [1, 4]:

$$\frac{T_{tc}-T_{sp}}{R_{sp-tc,r}}+\frac{T_{tc}-T_{sp}}{R_{sp-tc,c}}+\frac{T_{c}-T_{sp}}{R_{c-sp}}+\tau_{tc}G+Q_{atm}-Q_{rad}=0$$ * MERGEFORMAT

(4-1)

R_{c-sp} is the thermal resistance between TEG and sample plate, K/W; T_c is the temperature of TEG cold side, K; $\tau_{tc}$is the transmittance of transparent cover; Q_{rad} is the radiant energy of the radiant cooler, W/m^2; Q_{atm} is the heat absorbed from the atmosphere, W/m^2. R_{c-sp}, Q_{atm} and Q_{rad} are calculated as follows [2,5]:

$$R_{c-sp}=\frac{\sigma_{sp}}{k_{sp}A_{sp}}+\frac{\sigma_{GAF}}{k_{GAF}A_{GAF}}+\frac{\sigma_{ad}}{k_{ad}A_{ad}}+\frac{\sigma_{PI}}{k_{PI}A_{PI}}$$

$$Q_{atm}=2\int_0^{\infty}\int_0^{\pi/2}\varepsilon_s(\lambda,\theta)\cdot E_b(\lambda,T_a)\cdot\alpha_{sp}(\lambda,\theta)\cdot\tau_{tc}(\lambda,\theta)\sin\theta\cos\theta d\theta d\lambda$$ *

MERGEFORMAT (3-9)

$$Q_{rad}=\int_0^{\infty}\left[\frac{E_b(\lambda,T_{sp})\cdot(1-r_{tc,\lambda})-\varepsilon_{tc,\lambda}\cdot E_b(\lambda,T_{tc})}{\frac{1}{\varepsilon_{sp,\lambda}}-\left[\frac{(1-\varepsilon_{sp,\lambda})}{\varepsilon_{sp,\lambda}}\right]\cdot r_{tc,\lambda}}\right]d\lambda$$ * MERGEFORMAT

(3-10)

where σ_{sp}, σ_{GAF}, σ_{ad}, and σ_{PI} denote the thickness of the sample plate, GAF, adhesive layer and PI layer, m; k_{sp}, k_{GAF}, k_{ad} and k_{PI} are the thermal conductivity of the sample plate, GAF, adhesive and PI, W/(mK); A_{sp},A_{GAF},A_{ad} and A_{PI} are the area of the sample plate, GAF, adhesive and PI, m^2; $\varepsilon_s(\lambda,\theta)$ is the emissivity to the sky, rad; θ is the zenith angle, rad; λ is the wavelength, μm; $\alpha_{sp}(\lambda,\theta)$ is the absorptivity of the sample plate; $E_b(\lambda,T_a)$,$E_b(\lambda,T_{sp})$ and $E_b(\lambda,T_{tc})$ are the radiation power of the blackbody at environmental temperature, emitter temperature, and internal temperature respectively, W/(m^{2}μm); $\tau_{tc}(\lambda,\theta)$ is the transmittance of transparent membrane; $\varepsilon_{sp,\lambda}$ is the emissivity of the sample plate; $r_{tc,\lambda}$ and $\varepsilon_{tc,\lambda}$ are the reflectivity and emissivity of transparent membrane. Due to the huge amount of data, the calculation of $\varepsilon_s(\lambda,\theta)$ is very complex. Here, according to the derived formula, only the dew point temperature is input to calculate the effective sky emissivity ε_s. The calculation formula is as follows [6-8]:

$$\varepsilon_s=\begin{cases}0.727+0.0060(T_{dew}-273.15)\cdots daytime\\0.741+0.0062(T_{dew}-273.15)\cdots nighttime\end{cases}$$ * MERGEFORMAT (3-

11)

T_{dew} is the dew point temperature, K.

(3) The energy balance equation at the TEG cold end is as follows [9]:

$$Q_{teg-c} = 2n_{teg}ST_{cold}I + 2n_{teg}\frac{a_{teg}k_{teg}}{l_{teg}} \triangle T + \frac{1}{2}I^2 2n_{teg}\frac{r_{teg}l_{teg}}{a_{teg}}$$ * MERGEFORMAT (4-3)

Q_{teg-c} is the energy through the cold side of the TEG; T_{cold} is the temperature of the cold side of the TEG, K; n_{teg} is the number of PN junctions; S is the Seebeck coefficient, V/K; I is the current of the TEG, A; l_{teg} is the length of the TEG, m; r_{teg} is the resistivity of the TEG; a_{teg} is the cross-sectional area of the TEG leg, m^2.

(4) The energy balance equation at the TEG hot end is as follows [9]:

$$Q_{teg-h} = 2n_{teg}ST_{hot}I + 2n_{teg}\frac{a_{teg}k_{teg}}{l_{teg}} \triangle T - \frac{1}{2}I^2 2n_{teg}\frac{r_{teg}l_{teg}}{a_{teg}}$$ * MERGEFORMAT (4-4)

Q_{teg-h} is the energy passing through the hot end of the TEG; T_{hot} is the temperature of the hot end of the TEG, K. In the actual operation of the system, the TEG must be operated in a closed loop to transfer power to the external load. The heat flow of TEG includes heat conduction and Peltier heat, therefore $\triangle T$ is written as [10]:

$$\triangle T = (1 + ZT)(T_{teg-h} - T_{teg-c})$$ * MERGEFORMAT (4-5)

ZT is the quality factor of the thermoelectric device, which is expressed as [10]:

$$ZT = S^2\frac{\sigma}{k}\frac{T_{teg-h} + T_{teg-c}}{2}$$ * MERGEFORMAT (4-6)

σ is the electrical conductivity (S/m) and k is the thermal conductivity of the TEG (W/m/K).

(5) The VACNT-PMMA layer is assumed to be a blackbody with low emissivity and its thermal radiation is neglected. The heat flux through the PV cell to the VACNT-PMMA layer can be expressed as [11]:

$$\frac{(T_{VP} - T_h)}{R_{VP-h}} = \frac{(T_{pv} - T_{VP})}{R_{pv-VP}} + A_{VP}G\tau_{pv}$$ * MERGEFORMAT (4-7)

where, T_{VP} and T_{pv} are the temperatures of the VACNT-PMMA layer and the PV cell, °C. R_{VP-h} and R_{pv-VP} refer to the thermal conductive thermal resistances between the VACNT-PMMA layer and the hot end of the TEG and thermal conductive thermal resistances between the VACNT-PMMA layer and the photovoltaic cell, K/W. A_{VP} is the area of the VACNT-PMMA layer and τ_{pv} is transmittance of the PV cell.

(6) The energy balance equation of photovoltaic cells is as follows [12-14]:

$$Q_{sun-pv} = E_{pv} + Q_{pv-conv} + Q_{pv-rad} + Q_{pv-cond}$$ * MERGEFORMAT (4-8)

$$Q_{sun-pv} = (\alpha\tau)_{pv}A_{pv}I_s$$ * MERGEFORMAT (4-9)

$(\alpha\tau)_{pv}$ is the product of absorbance and transmittance of the PV cell , A_{pv} is the area of the PV cell and I_s is the direct radiation [12].

$$(\alpha\tau)_{pv} = \frac{\tau_\alpha\tau_\rho\alpha}{1 - (1 - \alpha)\rho_g}$$ * MERGEFORMAT (4-10)

The electrical output is written as[15]:

$$E_{pv} = (\alpha\tau)_{pv}A_{pv}I_s\eta_r[1 - \beta_r(T_{pv} - T_r)]$$ * MERGEFORMAT (4-11)

η_r is the standard efficiency of the PV cell, β_r is the temperature coefficient of the PV cell, T_{pv} is the temperature of the PV cell and T_r is the temperature under standard operating conditions.

$Q_{pv-conv}$ is the convective flow between the PV cell and the environment, which is written as:

$$Q_{pv-conv} = \frac{T_{pv} - T_a}{R_{pv-conv}}$$

* MERGEFORMAT (4-12)

R_{pv-c} is the convection thermal resistance between environment and PV cell , and the expression is as follows:

$$R_{pv-conv} = \frac{1}{(2.8 + 3u)A_{pv}}$$

* MERGEFORMAT (4-13)

u is the wind speed.

The energy transferred to space by radiation can be written as follows [12]：

$$Q_{pv-rad} = \frac{T_{pv} - T_{sky}}{R_{pv-rad}}$$

* MERGEFORMAT (4-14)

R_{pv-rad} is the radiation thermal resistance between sky and PV cell, T_{sky} is the sky temperature, which can be written as follows [3]：

$$R_{pv-rad} = \frac{1}{\sigma(T_{sky}^2 + T_{pv}^2)(T_{sky} + T_{pv})A_{pv}}$$

* MERGEFORMAT (4-15)

σ is the Boltzmann constant. T_{sky} can be given by:

$$T_{sky} = 0.0552T_a^{1.5}$$

* MERGEFORMAT (4-16)

$Q_{pv-cond}$ is the heat transfer between thermal conductive adhesive and PV cell, which is given by:

$$Q_{pv-cond} = \frac{(T_{adj} - T_{pv})}{R_{pv}}$$

* MERGEFORMAT (4-17)

T_{adj} is the temperature of the thermal conductive adhesive and R_{pv} is the thermal resistance between the thermal conductive adhesive and PV cell, which can be written as follows:

$$R_{pv} = \frac{\sigma_{pv}}{k_{pv}A_{pv}}$$

* MERGEFORMAT (4-18)

σ_{pv} and k_{pv} are the thickness of the PV cell and thermal conductivity.

Section 2. Design and manufacture of PV-TE-RC module system

The schematic diagram of the prepared self-electric device is shown in Figure 4a, and the physical diagram is shown in Figure 4b. The PV-TE-RC module consists of a radiation cooler, a thermoelectric panel, a PCL layer and an Infrared-Transparent Si PV Cell, and the main components are shown in S9. The radiant cooler is a GFA and RC composite film with a diameter of 80mm and a thickness of 0.4mm. The thermoelectric generator model is TEG-127365 and its dimensions are 40×40×3.8mm. The Infrared PV Cell is designed and manufactured with gate electrodes on both sides to form an infrared Transparent device that allows photons below the band gap to pass through. As shown in Fig S12, the transmittance of PV cell is ~30% in infrared band. The Infrared PV Cell measures 0.04 x 0.04 cm and has a calibrated efficiency of 18.9% under solar irradiation of 1000 W/m^2.Radiant coolers, thermoelectric generators and Infrared-Transparent Si PV cells are thermoformed in custom moulds to reduce heat loss in contact between layers.

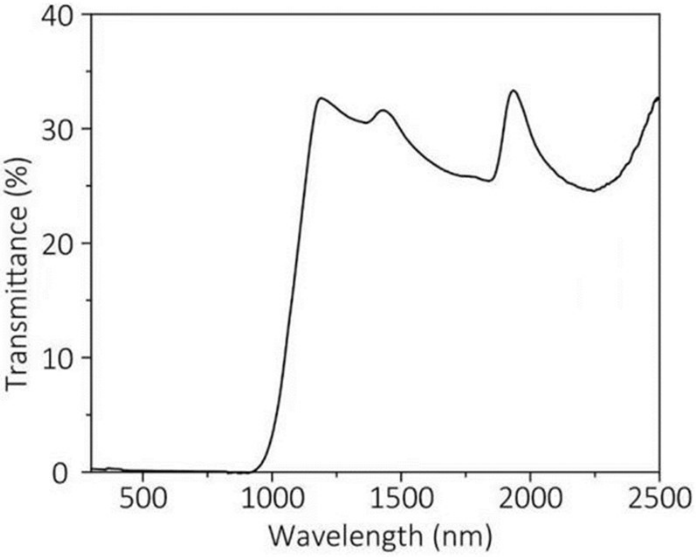

Fig S12. Photovoltaic cell transmittance.

Section 3. Design and manufacture of PV-TE-RC module test system

In the PV-TE-RC system, the key to improve the efficiency is the wide optical selectivity in the cooling range of solar irradiation to sky radiative cooling and the reduction of parasitic heat loss as much as possible. To reduce parasitic losses, we placed the PV-TE-RC module in a vacuum unit (Figure 4c). The vacuum device is mainly consisting of a vacuum chamber, an observation window, a support and a vacuum pump (see Fig S10). Welded bracket in vacuum chamber for supporting PV-RC-TE device. The top of the metal bracket is fitted with a quartz washer, which has a low venting rate. The contact area between quartz washer and radiant cooler is small, which can reduce the heat conduction. The heat transfer coefficient of the quartz washer is 1.3W/(m·K). In order to make the radiation cooler work efficiently, the top surface of the vacuum cavity should be a mid-infrared permeability window, and ZnSe glass plated with 8-13μm anti-reflection film on both sides is selected as the observation window of the top surface of vacuum cavity. The transmittance of coated ZnSe glass in the atmospheric window band is greater than 90%, ensuring that the radiative cooler can transmit heat radiation to the space. (See Fig S6) The radiation cooler not only emits heat radiation from the front, but also has radiation heat exchange with the vacuum chamber on the opposite side. Therefore, in order to reduce the radiation heat transfer between opposite side of sample and inner wall of the vacuum chamber, an anti-radiation screen with high reflectivity is added to the lower part of the radiation cooler. The anti-radiation screen group is composed of several polished aluminium plates connected by quartz washers, and holes are punched in its center to make PV-TE embedded in it. The anti-radiation screen group consists of five anti-radiation screens, the anti-radiation screen diameter is 80mm, the thickness is 1mm, and the quartz washer thickness is 1mm.

Section 4. Vacuum device components and their parameters

In this study, a small vacuum device is designed as shown in Fig S7. The device mainly consists of vacuum chamber, observation window, and vacuum pump. The cavity is made of stainless steel with a depth of 60mm and an inner diameter of 84mm. Four neck tubes are opened on the side wall of the cavity for air inlet and outlet, connecting to the vacuum pump, connecting to the thermocouple flange and connecting to the vacuum gauge. The observation window and the chamber are sealed by a rubber ring. The sealing effect between the observation window and the chamber is achieved by a rubber ring. The required high vacuum environment pressure of the chamber is 10^{-4}pa, and the working pressure of the commonly used mechanical pump is 10^{5} Pa-10^{-1}Pa. To achieve a high vacuum environment, it is necessary to form a unit with a diffusion pump to meet the demand of the chamber, and the working pressure of the diffusion pump is 10^{-1}Pa-10^{-4}Pa. In this study, the 2XZ-1 rotary vane vacuum pump of Linhai Yonghao Vacuum Equipment Co., Ltd. is used as the pre-stage pump (Fig S13.), the maximum power is 250W, the pumping rate is 1 L/S, and the ultimate vacuum is about 0.1Pa. The diffusion pump is a K100 metal-oil diffusion pump of Chengdu Nangguang Machinery Co., Ltd. the maximum power is 650W, the pumping rate is 300L/S, and ultimate vacuum is about 10^{-5} Pa. The vacuum chamber is connected to the vacuum pump by means of stainless-steel bellows. Brackets are welded inside the vacuum chamber to support the PV-TE-RC unit. A quartz washer is mounted on top of the metal bracket. The quartz gasket has a small contact area with the radiant cooler to minimize heat transfer. The bottom and top surfaces of vacuum cavity are equipped with observation windows, which are required to withstand a pressure of 1 atm, with thickness of 8mm and diameter of 100mm. The observation windows on the bottom surface of the vacuum cavity are made of low-iron glass, whose transmittance rate is greater than 90% in the solar radiation bands, which enables the hot end of the TEG to receive more solar energy. The observation window on the top surface of the vacuum chamber should be a selective transmittance window in the mid-infrared. In this study, ZnSe glass coated with 8-13 μm transmittance enhancement film on both sides is used as the observation window on the top surface of the vacuum cavity, and the spectral characteristics are shown in Fig S6.

Fig S13. 2XZ-1 type rotary vane vacuum pumps.

Section 5. Preparation of VACNT-PMMA film

Firstly, VACNT was synthesized on SiO_2 substrate by chemical vapor deposition process. The ferrocene and toluene solution with a concentration of 0.02 (g/ml) was evaporated at 200 °C, and then argon was introduced into the reaction zone and deposited at 800 °C for 30 minutes. The controllable diameter, length and orientation of nanotubes can be achieved by the above chemical vapor deposition process. Vertically aligned carbon nanotubes (VACNT) with a length of about 1 mm and a diameter in the range of 20~45 nm. The SEM images are shown in Fig S14 and Fig S15, revealing the cross-sectional microstructure of the original VACNT forest. Fig S14 shows the vertical arrangement of CNT growing in the forest (without any bending or buckling), and Fig S15 shows the top surface of VACNT.

For the preparation of VACNT-PMMA composite film, the VACNT sample was contacted with 20%wt PMMA and acetone mixed solution at one edge. Because of the high capillary force of CNT structure, PMMA enters VACNT forest structure under the action of capillary force to crosslink with CNT, and then evaporates acetone solvent after drying at 80°C for half an hour. After drying, the transferable VACNT-PMMA composite film can be obtained by simply cutting the film from SiO_2 substrate.

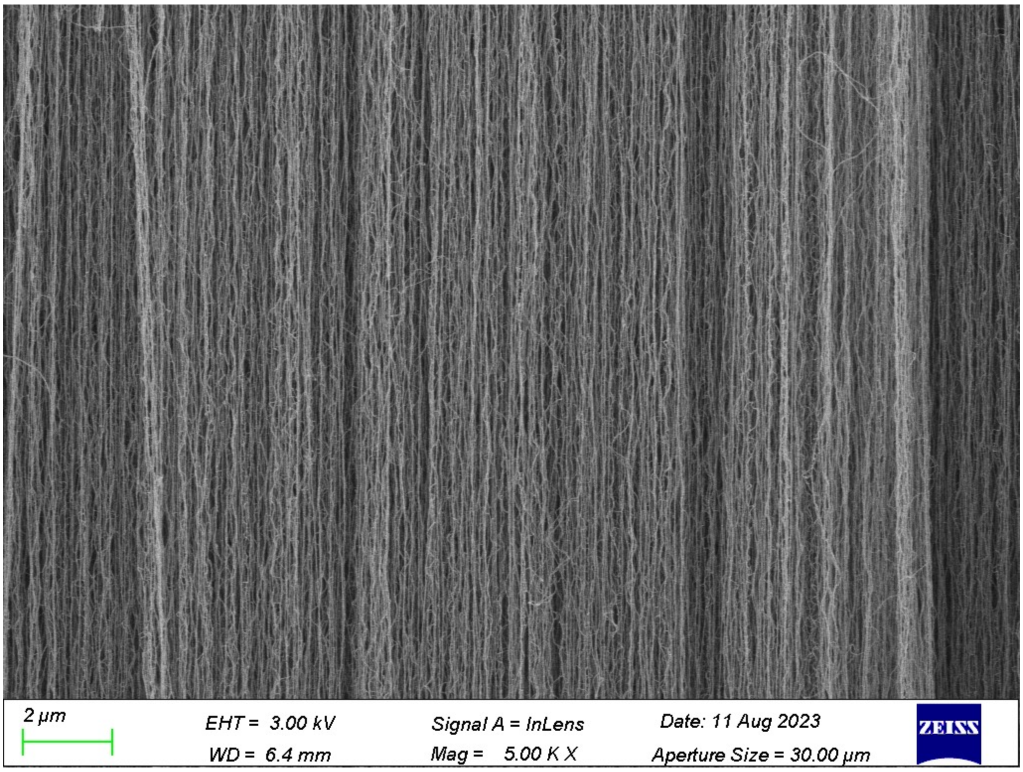

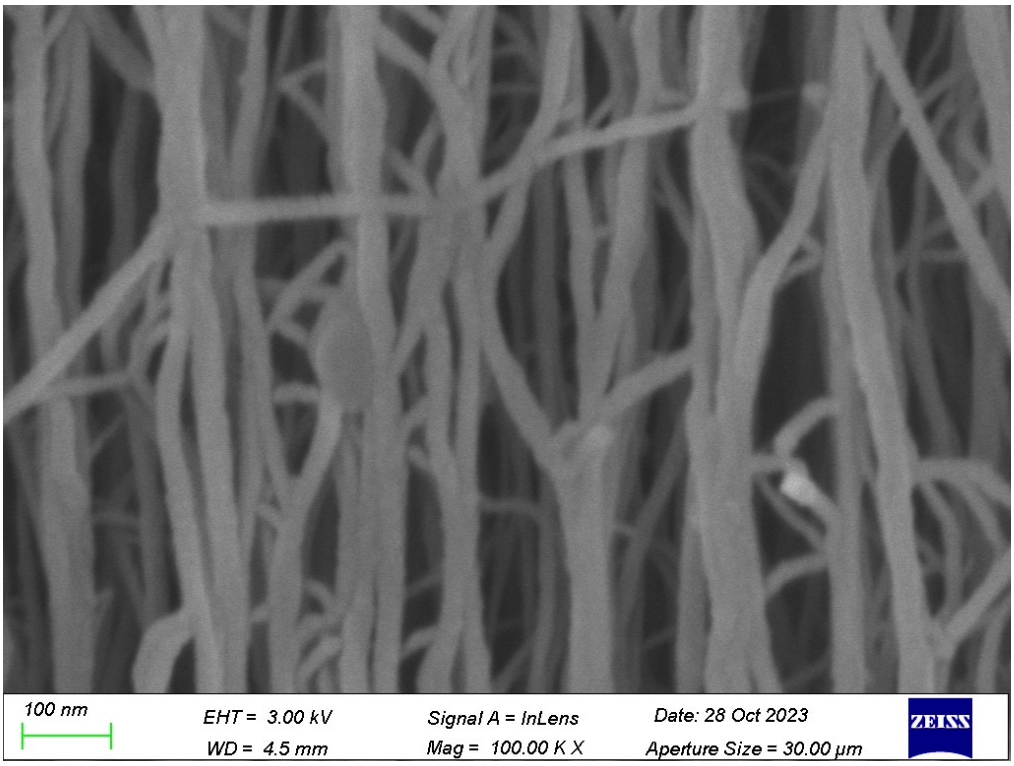

Figure 14. SEM image of VACNT cross section.

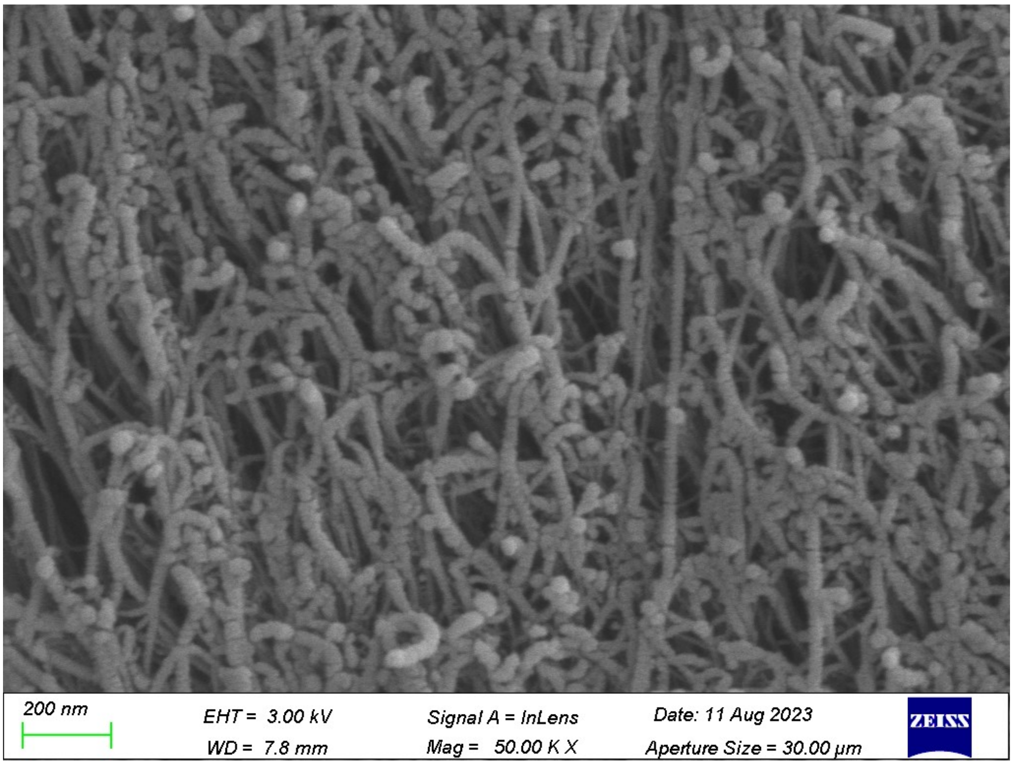

Fig S15. SEM image of VACNT top surface.

Section 6. Preparation of PDMS film, GAF film and GAF-PDMS film

Graphene assembled films (GAF) was prepared by a reduction method. The 20 mg/ml graphene oxide (GO) suspension was stirred to gel state and coated on the polyethylene terephthalate (PET) substrate. After drying at room temperature for 24 hours, it was annealed at 1200 ℃ and 2850 ℃ for 60 minutes in an argon annealing furnace. Finally, a flexible graphene assembly film with a thickness of 25μm was prepared by rolling process.

Preparation and doping modification of PDMS film: Firstly, the solution of PDMS (10 g) mixed with cyclohexane solution (20 g). Secondly, ZrO_2 powder (1g) and curing agent (1g) are added to the PDMS. Thirdly, the new PDMS mixture is stirred for 5 hours and heated for 1-2 minutes from time to time to make the PDMS and ZrO_2 mix evenly. Fourthly, the mixed solution was degassed ultrasonically for 10 min, and then the PDMS solution was spread on the deionized water-treated plate glass and scraped and coated into a film with a thickness of 100μm by means of a spatula. Finally, uniform ZrO_2/PDMS films were obtained after drying (80 °C) for 1 h to evaporate the cyclohexane.

GAF-PDMS composite films preparation: GAF-PDMS composite films were prepared by lamination method. The composite film was bonded with a pressure-sensitive thermally conductive spray adhesive (Spectrum 066), with the PDMS layer, the thermally conductive adhesive layer, and the graphene layer in order from top to bottom. Firstly, a graphene film with a thickness of 25μm was laid on smooth acrylic plastic film, and then spray the foggy thermal conductive adhesive at a constant speed perpendicular to the surface of the graphene film. When spraying, the nozzle was 30cm away from the graphene film, and the thickness of the thermal conductive adhesive was 20μm. The atomized thermal conductive adhesive is evenly laid on the surface of graphene film, and connected and stacked to form a uniform thermal conductive adhesive layer. After spraying the thermal conductive adhesive for 20s, the prepared PDMS film was quickly laid flat on the surface of the thermal conductive adhesive layer, and then a layer of smooth acrylic plastic film was covered on the surface of the PDMS film. The multilayer structure was then placed in a hot press at 80°C for 20 minutes, and the surface pressure was set to 1 kPa, which could enhance the bonding effect of the thermally conductive adhesive layer, so that the graphene film and the PDMS film were tightly bonded together. The hot-pressing time and surface pressure are affected by the adhesive layer. As the thickness of the adhesive layer increases, the hot-pressing time and surface pressure should also increase by a certain value to ensure the bonding effect of the adhesive layer. The acrylic plastic film can protect the film from damage and make the stress of the composite film uniform. The GAF-PDMS film was obtained by removing the surface acrylic plastic film after hot pressing.

Section 7. Graphene Assembled Film (GAF) Performance Testing and Characterization

The Fig S16a shows the microscopic surface image and the physical image of GAF, indicating good flexibility and many tiny folds on the surface. As shown in the XRD image of Fig S16b, the characteristic graphite peak of GAF is located at $2\theta = 26.5°$, and the diffraction peak (0 0 4) is of strong intensity, which indicates that GAF has a layer-stacked structure with a high degree of graphitization and an interlayer spacing of ~0.34 nm.The Raman spectrogram in Fig S16b shows in addition to the weak D-band and the strong G-band, which likewise indicates a high degree of graphitization of GAF. As shown in the SEM image of Fig. S17, the GAF film thickness is ~26μm and has a layer stacking structure. As shown in Fig 16c, the IR image indicates that the thermal conductivity of GAF is much higher than that of copper foil.

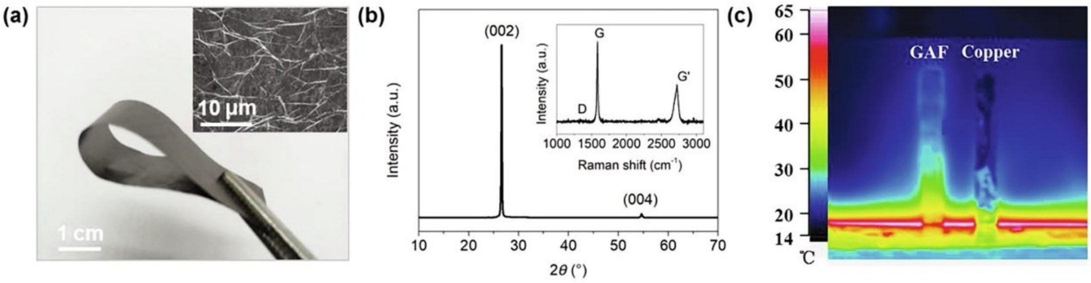

Fig S16. Characteristic of GAF

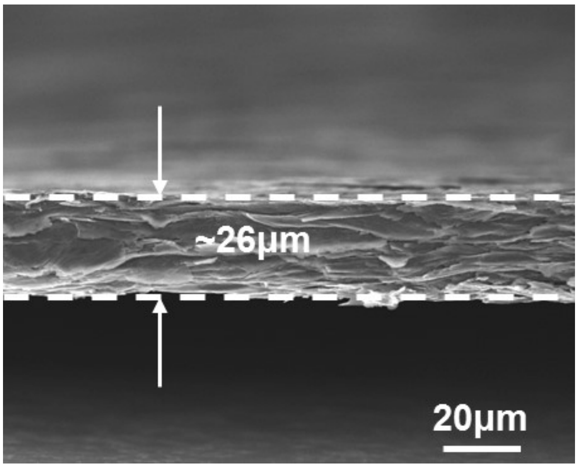

Fig S17. Cross-section SEM image of GAF

Thermal conductivity measurements:

Measurement of thermal conductivity of GAF and Cu foil by ASTM E1461 method (NETZSCH LFA 467). The samples were cut into round shapes with a diameter of 2.5 cm. Then, we can obtain thermal diffusivity by the following equation:

$$\alpha = 0.1388d^2(t_{50})^{-1}$$

Where d is the thickness, α is the thermal diffusivity, t_{50} is half of the time when the surface temperature of the sample rises to the maximum temperature. The calculation formula of thermal conductivity is as follows:

$$K = \rho C_p \alpha$$

Where ρ is the density, C_P is the specific heat capacity. Physical properties of GAF and Cu foil are shown in Table 1, in which the properties of Cu can be found in http://www.matweb.com/.

Table 1. Physical properties of GAF and Cu foil

Materials	Thickness (μm)	Density (cm^{-1})	Specific heat capacity (g^{-1}•K^{-1})	Thermal diffusivity (mm^2•s^{-1})	Thermal conductivity (W•m^{-1}•K^{-1})	Coefficient of thermal expansion (K^{-1})
GAF	25	2.1	0.76	798.12	1273.8	-8 to -1.5
Cu foil	25	8.9	0.39	98.466	341.8	16.4

References

[1] Hu MK, Zhao B, Suhendri, Cao JY, Wang QL, Riffat S, et al. Feasibility of realizing daytime solar heating and radiative cooling simultaneously with a novel structure. Sustain Cities Soc. 2021;74.

[2] Hu MK, Zhao B, Li J, Wang YY, Pei G. Preliminary thermal analysis of a combined photovoltaic-photothermic-nocturnal radiative cooling system. Energy. 2017;137:419-30.

[3] Zhao B, Hu MK, Xuan QD, Kwan TH, Dabwan YN, Pei G. Tunable thermal management based on solar heating and radiative cooling. Sol Energ Mat Sol C. 2022;235.

[4] Hu MK, Zhao B, Ao XZ, Chen N, Cao JY, Wang QL, et al. Feasibility research on a double-covered hybrid photo-thermal and radiative sky cooling module. Sol Energy. 2020;197:332-43.

[5] Zhao HP, Zhan YH, Dou SL, Wang L, Li Y, Li XF. Passive radiative temperature regulator: Principles and absorption-emission manipulation. Sol Energ Mat Sol C. 2021;229.

[6] Vall S, Castell A. Radiative cooling as low-grade energy source: A literature review. Renew Sust Energ Rev. 2017;77:803-20.

[7] Zhao DL, Aili A, Zhai Y, Xu SY, Tan G, Yin XB, et al. Radiative sky cooling: Fundamental principles, materials, and applications. Appl Phys Rev. 2019;6(2).

[8] Raman AP, Li W, Fan SH. Generating Light from Darkness. Joule. 2019;3(11):2679-86.

[9] Liao TJ, He QJ, Xu QD, Dai YW, Cheng C, Ni M. Coupling properties and parametric optimization of a photovoltaic panel driven thermoelectric refrigerators system. Energy. 2021;220.

[10] Ji Y, Lv S. Comprehensive research on a simple and efficient radiative cooling driving thermoelectric generator system for nighttime passive power generation. Appl Therm Eng. 2023;219:119560.

[11] Ji Y, Lv S, Qian Z, Ji Y, Ren J, Liang K, et al. Comparative study on cooling method for concentrating photovoltaic system. Energy. 2022;253:124126.

[12] Yazdanifard F, Ebrahimnia-Bajestan E, Ameri M. Investigating the performance of a water-based photovoltaic/thermal (PV/T) collector in laminar and turbulent flow regime. Renew Energ. 2016;99:295-306.

[13] Yin XB, Yang RG, Tan G, Fan SH. Terrestrial radiative cooling: Using the cold universe as a renewable and sustainable energy source. Science. 2020;370(6518):786-+.

[14] Liao TJ, Xu QD, Dai YW, Cheng C, He QJ, Ni M. Radiative cooling-assisted thermoelectric refrigeration and power systems: Coupling properties and parametric optimization. Energy. 2022;242.

[15] Yousef MS, Rahman AKA, Ookawara S. Performance investigation of low - Concentration photovoltaic systems under hot and arid conditions: Experimental and numerical results. Energ Convers Manage. 2016;128:82-94.